Overview of the Integrated Adaptive Wing Technology Maturation Wind-Tunnel Test Objectives

Patrick S. Heaney*
NASA Langley Research Center, Hampton, VA, 23681

John F. Quindlen†
Boeing Research & Technology, Huntington Beach, CA, 92647

The Integrated Adaptive Wing Technology Maturation wind-tunnel test is the culmination of a cooperative effort between NASA and Boeing to develop control techniques that can improve the performance and safety of higher aspect ratio flexible transport aircraft. The wind-tunnel test article, to be tested at the NASA Langley Research Center Transonic Dynamics Tunnel, is a semispan model of a modern transport configuration based on the NASA Common Research Model with an aspect ratio 13.5 wing. Multiobjective control laws have been developed targeting drag optimization, maneuver load alleviation, gust load alleviation, and active flutter suppression. In this paper, the integrated model design, active control system, and sensor suite will be presented, and pretest modeling and characterization activities will be described. A summary of the planned wind-tunnel test entries will provide an overview of the experimental approach and expected outcomes.

Nomenclature

f	=	frequency
g	=	damping
h	=	altitude
p_i	=	initial wind-off pressure
M_∞	=	freestream Mach number
q_∞	=	freestream dynamic pressure
Re_c	=	chord Reynolds number

I. Introduction

One of the primary objectives of the Integrated Adaptive Wing Technology Maturation (IAWTM) activity, a cooperative effort between NASA and Boeing, is to design and test an integrated wing concept that, through the use of active adaptive technologies, optimizes drag and weight for a next generation, high aspect ratio, flexible wing. Within the NASA Advanced Air Transport Technology (AATT) project, the IAWTM effort supports the NASA Higher Aspect Ratio Optimal Wing technical challenge of enabling a 1.5 to 2 times increase in the aspect ratio of a thin, lightweight wing while maintaining safe flight control and structures. To achieve this objective, IAWTM aims to develop control techniques to improve vehicle performance by reducing induced drag and structural weight penalties, and demonstrate performance improvements with a representative wind-tunnel (WT) experiment. Closed-loop control performance objectives will target drag optimization, maneuver load alleviation, gust load alleviation, and active flutter suppression. By developing techniques that will enable higher aspect ratio flexible wings, reductions in the environmental and financial cost of vehicle operation can be achieved.

The vehicle configuration that has been adopted for this project is a modern transport configuration with an aspect ratio 13.5 wing developed by the University of Michigan and based on the Common Research Model (CRM) [1], which is a 1.5 times increase over the nominal aspect ratio 9 NASA CRM wing [2]. A detailed description of the test article design, and configurations that will be tested during the experiment, is provided in Section III.A.

*Research Aerospace Engineer, Aeroelasticity Branch, MS 340, AIAA Member.
†Guidance, Navigation, & Control Engineer, Vehicle Dynamics and Controls, AIAA Member.

II. Background

Research activities under the IAWTM project have included the design and analyses of both full- and model-scale vehicles. In the first stage of the project, a high fidelity six degree of freedom dynamic aeroservoelastic (DASE) model was developed by Boeing and used extensively for evaluation of the simulated multiobjective control law performance. Trade studies were also conducted to identify and evaluate enabling technologies for meeting the challenges of designing and flying a higher aspect ratio wing. Significant performance improvements were demonstrated on the full-scale vehicle simulations using closed-loop controllers developed to meet the drag optimization, manuever and gust load alleviation, and active flutter suppression objectives.

Following a similar design philosophy as previous aeroelastic WT models, the initial model-scale work focused on developing a WT test article that would be used to demonstrate performance improvements on those closed-loop control objectives and validate the integrated wing concept during a WT experiment at the NASA Langley Research Center (LaRC) Transonic Dynamics Tunnel (TDT). The WT test article, designed and fabricated by NextGen Aeronautics, is a semispan, sidewall mounted, dynamically-scaled model with a spar-pod wing, flow-through engine nacelle, and nonmetric fuselage. The test article has ten active control surfaces along the trailing edge and a large number of sensors that will be used during testing, to include accelerometers, strain gauges, distributed strain sensors, and a 5-component strain gauge balance. The WT experiment will support the IAWTM project by demonstrating controllers that meet the following objectives:

1) Drag optimization at off-nominal conditions
2) Maneuver load alleviation (MLA)
3) Gust load alleviation (GLA)
4) Active flutter suppression (AFS)

The active controllers developed to meet these objectives have been implemented using MATLAB®, Simulink®, and dSPACE real-time hardware and software[1].

III. Wind-tunnel Test Article

A. Design

Initial sizing of the IAWTM WT test article was based on the desire to aeroelastically scale mass and stiffness distributions from the target full-scale vehicle to a semispan WT model that would be tested in the NASA LaRC TDT. Several aerodynamic scale factors for the WT test article are summarized in Table 1 for the selected cruise condition of Mach number (M_∞) 0.85, altitude (h) of 33,000 ft, and freestream dynamic pressure (q_∞) of 277 psf. The Reynolds number, Re_c, is based on the reference chord.

Table 1 Summary of IAWTM WT test article scale factors at the design cruise condition.

Parameter	Full-scale	Model-scale / Full-scale
Mach number	0.85	1
Dynamic pressure	277 psf	1
Velocity	834 ft/sec	0.560
Reynolds number	41×10^6	0.234
Reference chord	227 in	0.108
Reference span	236 ft	0.054
Reference area	4130 ft^2	0.005832

Figure 1a provides an illustration of the overall test article design. Carbon fiber skins attach to the spar via aluminum ribs to provide the aerodynamic shape, and the primary load path goes through the wing root attached to the mounting box assembly, shown in yellow, and the balance, shown in green. The fuselage is formed with a centerline rib, several bulkheads, and fiberglass skins. Since the fuselage is nonmetric, it is not scaled from the nominal full-scale aircraft fuselage length. The spar, with a sweep angle of 35-degrees, was sized to fit within the 16-ft TDT test section; the

[1]The use of trademarks or names of manufacturers in this paper is for accurate reporting and does not constitute an official endorsement, either expressed or implied, of such products or manufacturers.

overall dimensions of the test article are shown in Fig. 1b. The wing skins, forming the outer mold line (OML), are segmented into pods to minimize load transfer through the skin and reduce their relative stiffness impact. During testing, the pods will be taped to close out the air gaps.

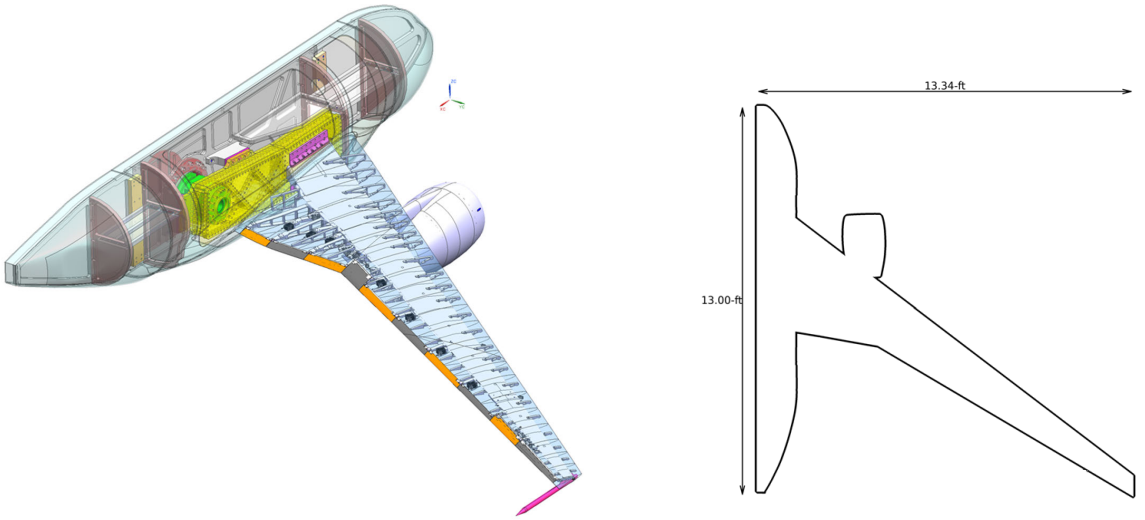

(a) WT test article with transparent skins to illustrate internal components [Source: Boeing]

(b) Overall WT test article dimensions

Fig. 1 Overview of the WT test article.

To dynamically scale the wing structure, an equivalent beam model of the spar was created to provide the target bending (EI) and torsional (GJ) stiffness distributions along the span of the wing. Based on cost and experience with similar WT models, 7075-T6 aluminum was chosen as the material to fabricate the spar. Using the equivalent beam model and these material properties, the target area moments of inertia were computed at 25 evenly-spaced design points along the elastic axis of the wing. During the iterative design process, a modified I-beam cross section, shown in Fig. 3c, was developed to improve stiffness matching while remaining inside the wing OML. The target and design area moments of inertia at the design points are presented in Fig. 2, where it can be seen that some target moments of inertia were not feasible due to OML constraints.

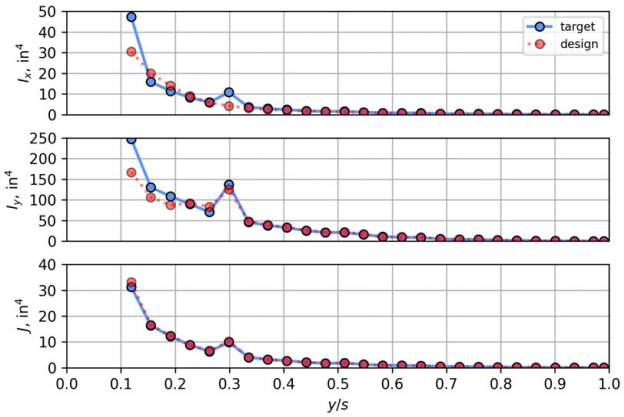

Fig. 2 Comparison of spar sectional target and designed area moments of inertia.

The final spar design is presented in Fig. 3, where the complexity of the running cross section dimensions can be seen. A linear taper defines the spar dimensions between the design point cross sections. Due to the length of the spar, it was fabricated in two sections to improve ease of fabrication and reduce overall cost, and the two pieces were permanently bonded and fastened together at a spar joint, which is annotated in Fig. 3a.

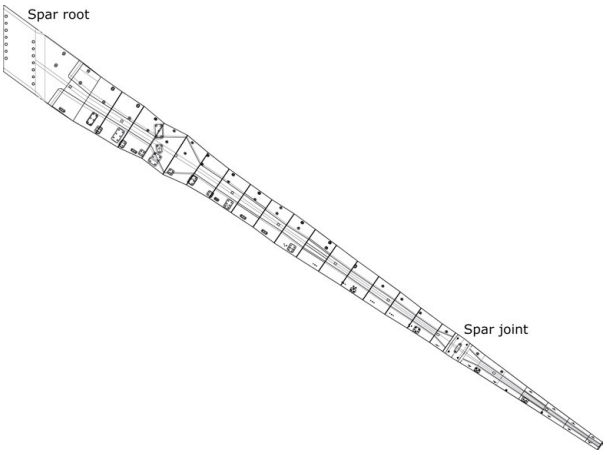

(a) Planform view illustrating the running sectional modified I-beam flange and webbing widths

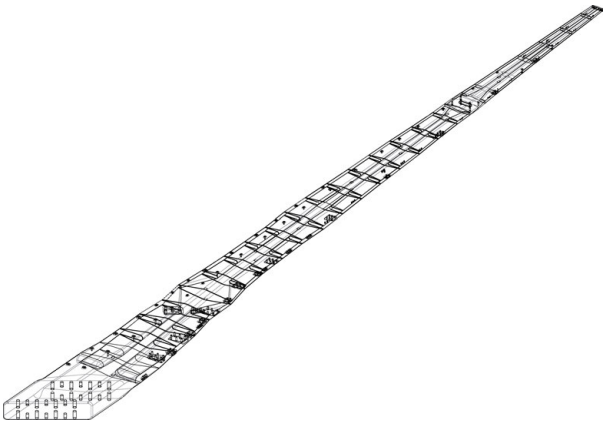

(b) Rotated view illustrating the running cross sections of the modified I-beam design

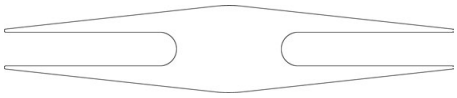

(c) Representative spar cross section located at approximately midspan

Fig. 3 WT test article spar design.

To support both aerodynamic performance testing using a balance and dynamic aeroelastic testing, the test article was designed such that the balance can be engaged and disengaged from the load path using a set of four shims. Figure 4 provides an illustration of the two configurations:

1) shims-off, with the load path from the wing, to the mounting box assembly (MBA), to the balance, and ending at the adapter drum, which is mounted to the TDT sidewall support hardware
2) shims-on, with the load path from the wing, to the MBA, to four mounting feet arranged on the four sides of the MBA, to the fuselage centerline plate, and ending at the adapter drum

To change from the shims-off to the shims-on configuration, a set of four shims are inserted between the mounting feet and the MBA, and the MBA is fastened to the fuselage centerline plate through these shims and mounting feet. After the balance fasteners are removed, the balance is no longer on the load path and the mounting feet carry the load from the MBA to the fuselage centerline plate. These two configurations will enable the acquisition of aerodynamic performance data using the balance during lower risk and less dynamic test conditions, as well as dynamic aeroelastic test data with the balance off the load path.

To support demonstration of AFS, a third test article configuration includes a removable tip ballast (shown in pink in Fig. 1a) to lower the flutter frequency and dynamic pressure. Late in the test article design, the predicted flutter dynamic pressure boundary for the shims-on configuration was determined to be too high for flutter testing due to test article safety limits. The tip ballast modification was designed in collaboration with NextGen Aeronautics to add a reasonably sized tip ballast that would lower the predicted flutter dynamic pressure. Based on preliminary conceptual sizing, two interchangeable tip ballasts were designed and built with adjustable fore-aft installation locations for modifying the dynamic aeroelastic stability of the test article. Subsequent analyses indicated that the aft-most position is most favorable for meeting the test objectives, and all test article structural characterization activities and aeroelastic modeling have been conducted for this tip ballast location. The tip ballast will only be installed during the characterization test runs for this configuration (described briefly below) and the AFS test runs.

The WT test article has ten trailing edge control surfaces, represented in Fig. 5, that will be used to meet the multiobjective control goals. Three of these control surfaces are hydraulically-actuated ailerons for increased bandwidth, and seven surfaces are miniplain flaps (MPFs) actuated with electric servos. The hydraulically-actuated control surfaces are controlled with Moog E024 servo valves and E085 linear hydraulic actuators operating through bell crank assemblies, and the MPFs are actuated by Dynamixel XM430-W210R servos. The supply pressure for the test article hydraulic system is 3,000 psi.

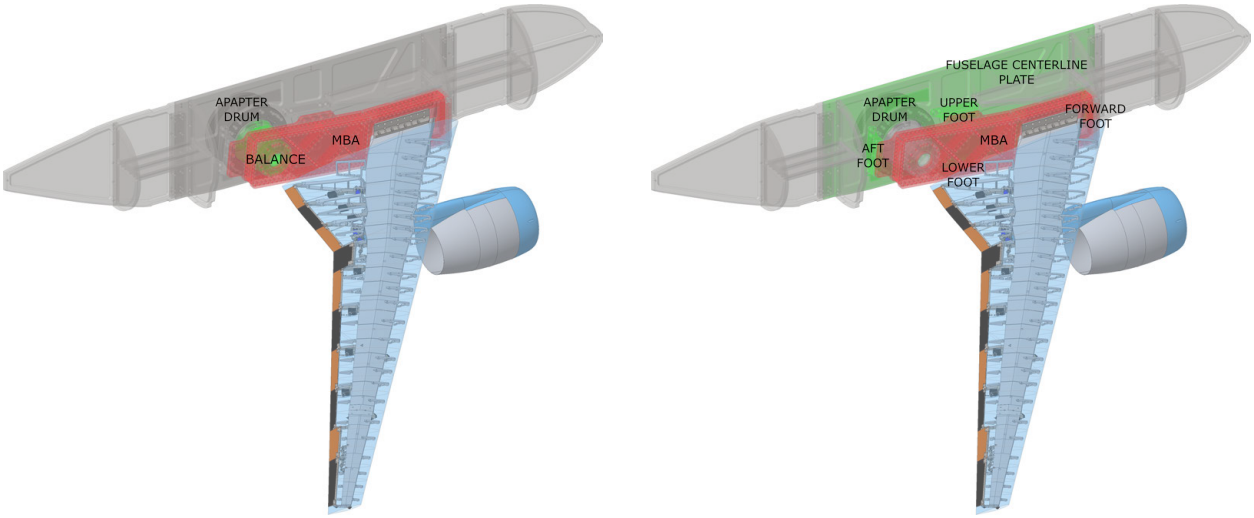

(a) Shims-off configuration **(b) Shims-on configuration**

Fig. 4 WT test article mount structural configurations.

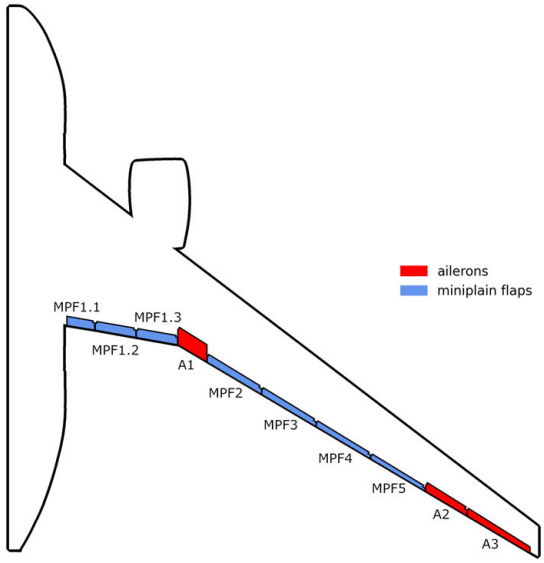

Fig. 5 WT test article control surfaces.

The test article is instrumented with a variety of sensors, to include three triaxial and 13 single axis accelerometers, ten full-bridge strain gauges, three fiber optic distributed strain sensing lines [3], a Q-flex inclinometer, and a five component balance (NASA balance 1637S). Locations instrumented with accelerometers are annotated in Fig. 6a and strain gauge locations in Fig. 6b. These sensors will be used during WT testing for test article safety and stability tracking, as well as for closed-loop control.

After delivery of the WT test article from NextGen Aeronautics in February 2021, buildup and checkout activities were conducted in the NASA LaRC TDT model preparation area. Photos of the WT test article during check out on the backstop in the model preparation area are shown in Fig. 7.

B. Aerodynamic and Aeroelastic Modeling

Significant modeling and analyses have been completed in support of the IAWTM WT test. Several CFD studies have been completed using FUN3D [4], to include simulations to compare rigid and flexible aerodynamics and critical

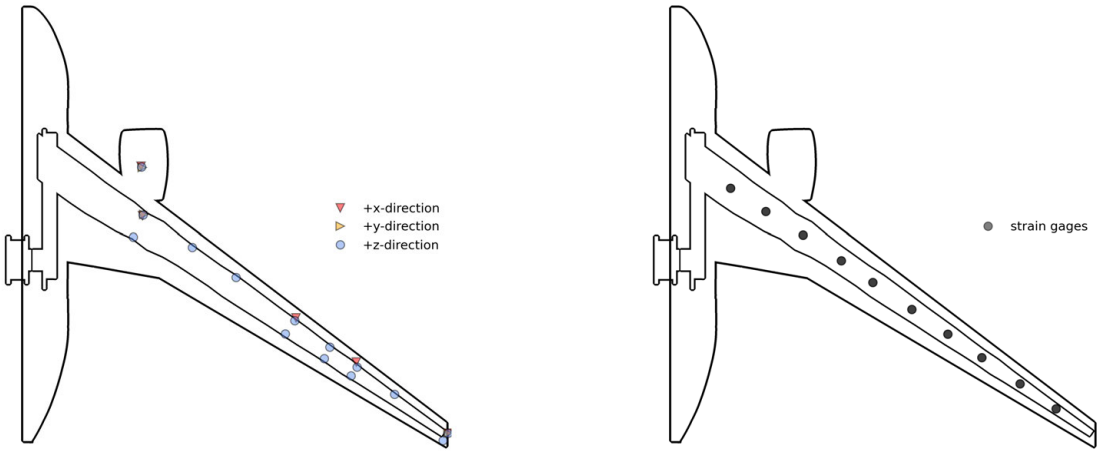

(a) Accelerometers **(b) Strain gauges**

Fig. 6 WT test article instrumentation.

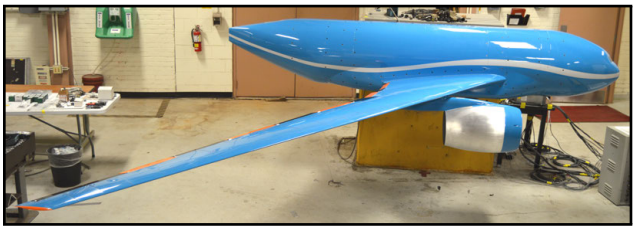

(a) Side view

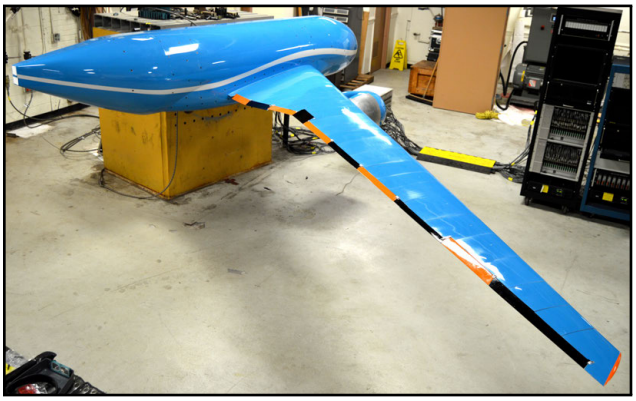

(b) View from aft

Fig. 7 WT test article installed on backstop in NASA LaRC TDT model preparation area [Source: NASA].

M_∞, estimate predicted flutter boundaries [5], assess the impact of WT wall interference, model the wake downstream of the TDT airstream oscillation system (AOS) [6], estimate the buffet onset angle of attack, estimate the predicted control surface reversal boundary, and improve adaptive mesh refinement techniques at transonic conditions for highly flexible structures [7]. VSPAERO has also been used to generate a control surface aerodynamic database for model-scale simulations [8, 9].

Aeroservoelastic (ASE) models have been developed using several methods and tools, to include unsteady doublet-lattice method (DLM) rational function approximations (RFAs) using ZAERO, unsteady vortex-lattice method (VLM) using VSPAERO, linearized frequency-domain (LFD) using FUN3D, and linearized reduced order model (ROM) using FUN3D [5]. ZAERO has been employed extensively to generate state-space models for control law development, which have been used to update and simulate control laws in Simulink® before compiling in dSPACE for WT test

integration. These model-based control laws, developed by Boeing and NASA [10, 11], will be updated throughout the characterization phase of the project as improved structural, control system, and aerodynamic models are developed.

The main tools for open loop stability analyses have been MSC Nastran [12] and ZAERO [13], which have been used to generate predicted flutter boundaries for the three WT test article configurations. Representative figures for the flutter analyses completed are shown in Fig. 8 for the shims-off configuration at $M_\infty = 0.85$, and in Fig. 9 for the shims-on, ballast-on configuration at $M_\infty = 0.70$. In the upper pair of plots in each figure, the modal frequency and damping versus q_∞ are plotted for 24 structural modes, and the lower figure presents the flutter mode shape with the color contour map proportional to out-of-plane displacement. For the shims-off configuration, the hump mode flutter mechanism occurs at $q_\infty \approx 212$ psf with a flutter frequency of $f \approx 7.35$ Hz. The flutter behavior for the shims-on, ballast-off configuration is generally quite similar to the shims-off configuration, with a slightly higher predicted flutter dynamic pressure and frequency at $M_\infty = 0.85$ ($q_\infty \approx 249$ psf and flutter frequency of $f \approx 7.56$ Hz). The shims-on, ballast-on configuration (Fig. 9), on the other hand, has a hard flutter mechanism at this M_∞ that is predicted to occur at $q_\infty \approx 170$ psf with a flutter frequency of $f \approx 6.01$ Hz. Numerical simulations using FUN3D have also been leveraged to compare predicted flutter boundaries using higher-fidelity aerodynamic models. Following the structural model updates that are currently underway based on the test section ground vibration test (discussed below), stability analyses as well as ASE models will be regenerated in ZAERO using the fully updated finite element model, with spot checks also planned using FUN3D.

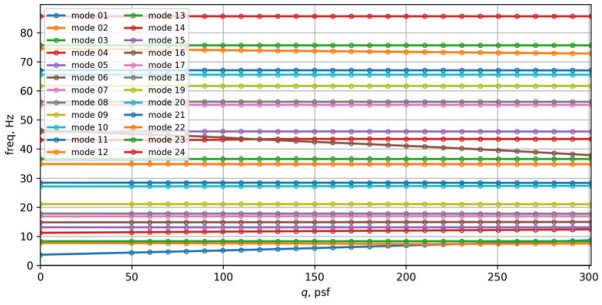

(a) Frequency versus q_∞

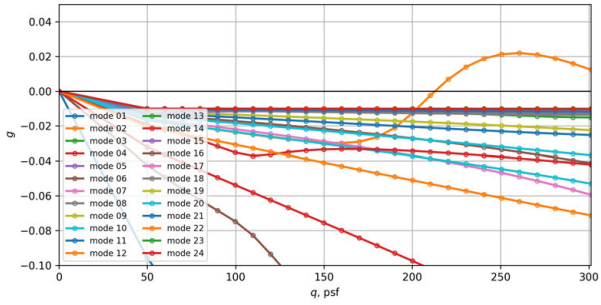

(b) Damping versus q_∞

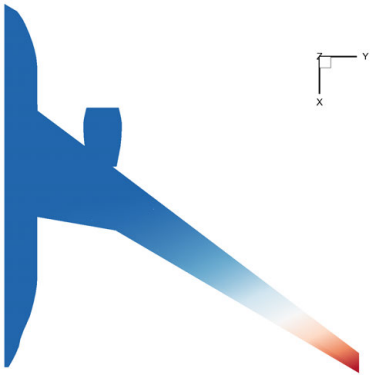

(c) Flutter mode shape, contours correspond to out-of-plane displacement

Fig. 8 Shims-off configuration at $M_\infty = 0.85$.

C. Characterization

Experimental characterization of the WT test article and model verification are essential tasks in support of the WT experiment. Several efforts have been completed to improve the pretest structural and control system models, to include:

1) generating a measured mass properties database
2) conducting actuator performance characterization testing
3) statically loading the spar for sensor calibration and model validation
4) conducting a ground vibration test (GVT) with the test article mounted to the model preparation area backstop
5) conducting a follow-on GVT with the test article installed on the TDT sidewall mount

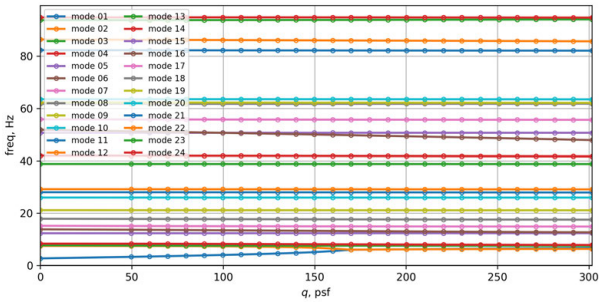

(a) Frequency versus q_∞

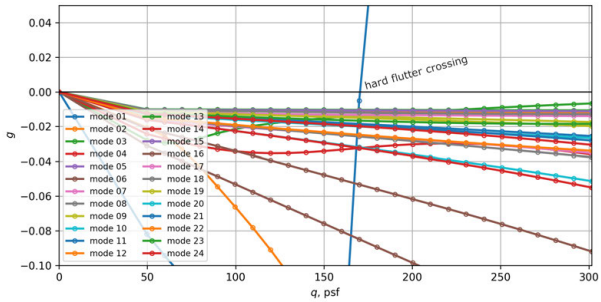

(b) Damping versus q_∞

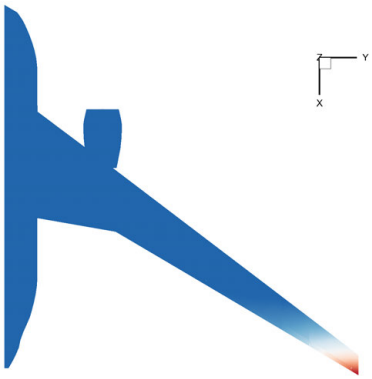

(c) Flutter mode shape, contours correspond to out-of-plane displacement

Fig. 9 Shims-on, ballast-on configuration at $M_\infty = 0.70$.

Wind-on aerodynamic characterization, to be conducted during the first WT entry, will also be used to update the structural, control system, and aerodynamic models in preparation for the closed-loop portion of the WT experiment.

Two of the most significant pretest characterization activities have been the backstop GVT, completed in the model preparation area of the TDT in June and July 2022, and the test section GVT, completed with the test article installed in the TDT in May and June 2023. All three test article configurations were tested during both tests, and several other parameters were varied to assess their modal impact. The more extensive parameter studies were conducted during the backstop GVT, to include taping the control surfaces or powering the actuators, leaving the pod gaps open or taping between, and using shakers or a hammer for excitation. In addition to the internal WT test article sensors, shown in Fig. 6, significant instrumentation was added externally to the model during these tests to characterize and improve the as-built finite element model (FEM) using experimental data. Figure 10 presents the WT test article as it was instrumented during the backstop GVT.

Fig. 10 WT test article instrumented with external accelerometers during the backstop GVT [Source: NASA].

Based on the data acquired during the backstop GVT, several updates were made to the FEM to more accurately represent the as-built test article, and significant improvements to the FEM-to-GVT cross-orthogonality and frequencies were achieved. Table 2 summarizes the FEM-predicted shims-off and shims-on modes for the test article mounted in the TDT test section after the FEM update based on the backstop GVT data.

Table 2 Summary of IAWTM WT test article FEM flexible modes for the ballast-off configurations in the TDT test section (modes important to model the predicted flutter mechanisms are marked in bold).

Shims-off		Shims-on		Description
Index	f (Hz)	Index	f (Hz)	
1	**3.63**	**1**	**3.65**	Wing 1st Vertical Bending
2	**7.67**	**2**	**7.92**	Vehicle Pitch
3	8.28	3	8.45	Wing 1st Fore-Aft Bending
4	**11.20**	**4**	**11.25**	Wing 2nd Vertical Bending
5	13.11			Fuselage 1st Side Bending
6	**14.80**	**5**	**14.93**	IB Wing Torsion, Wing 2nd Vertical Bending Inplane
7	**16.85**	**7**	**17.12**	IB Wing Torsion, Wing 2nd Vertical Bending Out of plane
8	**17.80**	**6**	**15.19**	Wing 2nd Fore-Aft Bending
9	**21.07**	**8**	**21.14**	Nacelle Side Bending
10	27.16	9	27.69	Wing 3rd Vertical Bending
11	**28.45**	**10**	**28.72**	Electric turntable axial
12	34.87			Fuselage Roll Bending, Wing 2nd Fore-Aft
13	36.61	11	36.53	Wing 3rd Fore-Aft Bending, Fuselage Side Bending Out of plane
		12	43.12	Wing 3rd Fore-Aft Bending, Fuselage Side Bending Inplane
14	43.08	**13**	**43.95**	Wing 4th Vertical Bending
15	**45.73**			Wing 3rd Fore-Aft Bending, Wing 1st Torsion
16	**46.44**	**14**	**46.35**	Wing 1st Torsion

Following the backstop GVT, the most significant uncertainties in the structural model for the WT test article mounted in the TDT test section are the electric turntable (ETT) and oscillating turntable (OTT) support structure models that form the boundary condition to which the test article will be mounted (shown in Fig. 11). Originally, a limited GVT was planned to be conducted immediately prior to wind-on testing during the first WT test entry, with data acquired during this test to be used to update the TDT mounting hardware FEM. Fortunately, an opening in the WT test schedule permitted the installation of the IAWTM test article in the TDT to conduct a more extensive test section GVT. In preparation for this test, ZAERO models were analyzed to identify a reduced subset of modes for each configuration that are required to retain the same flutter mechanisms as the full mode set. At the design condition, generalized aerodynamic forces (GAFs) are computed with the backstop-updated FEM, a density sweep and pk-solver is used to compute the eigensolution, and a subset of structural modes is manually identified that qualitatively retains the desired flutter mechanisms. Examples for both the shims-off and shims-on case are shown in Fig. 12, where the reduced mode set corresponds to modes in Table 2 in bold text. These reduced sets of modes were then identified as target modes for the test section GVT, which guided the planning for sensor and excitation placement. Figure 13 presents the WT test article installed in the TDT during the test section GVT. Model updating, targeting the TDT sidewall support hardware, based on data acquired during this GVT is currently underway.

IV. Test Plan

In this section, an overview of the IAWTM WT test plan is provided. Phase 1 testing will focus on open-loop characterization of the test article, and phase 2 will focus on the closed-loop performance demonstrations for controllers targeting each of the four objectives discussed above. An overview about test article and facility constraints limiting the test envelope is also presented.

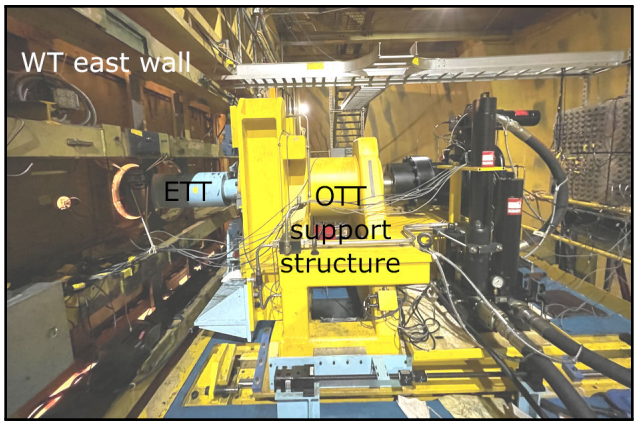

Fig. 11 Oscillating turntable (OTT) support structure and electric turntable (ETT) to which the WT test article will be mounted during the TDT test [Source: NASA].

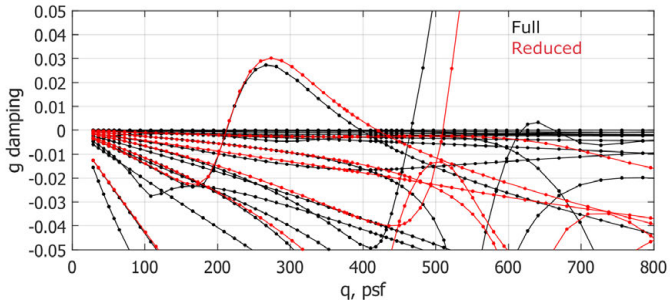

(a) Shims-off configuration

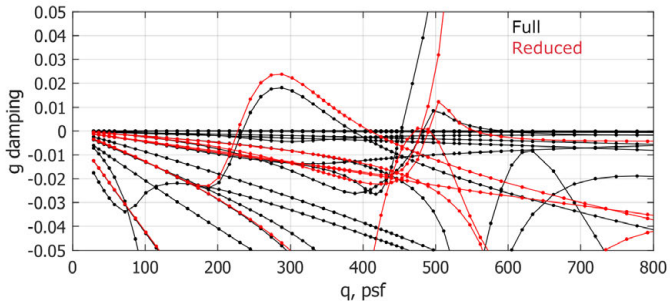

(b) Shims-on configuration

Fig. 12 Representative comparisons of modal damping as a function of dynamic pressure for full and reduced models. Reduced models include the mode subset identified in Table 2 with bold text.

A. Transonic Dynamics Tunnel

The TDT, shown in Fig. 14 with major components annotated, is a unique WT facility that contains several features essential for aeroservoelastic testing of the IAWTM WT test article. While the tunnel can operate in air, the heavy gas (R134a) test medium is essential to match fluid-structure scaling parameters important to aeroelastic response and flutter. The TDT is also configured to perform higher risk aeroelastic testing, with direct view of the test article from the control room, bypass valves that can rapidly lower test section dynamic pressure in the case of an instability, and downstream safety screens to protect the drive motor and fan blades. Hydraulic power supply for the test article is also available for high speed actuation of control surfaces, and an airstream oscillation system (AOS) with upstream gust vanes is available to provide gust excitation for GLA testing.

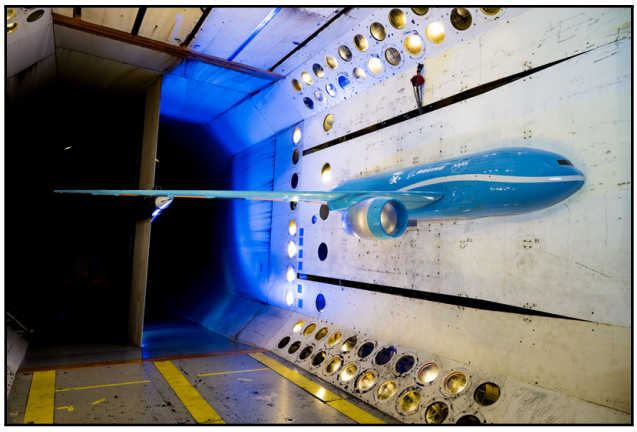

Fig. 13 WT test article installed in the TDT during the test section GVT [Source: NASA].

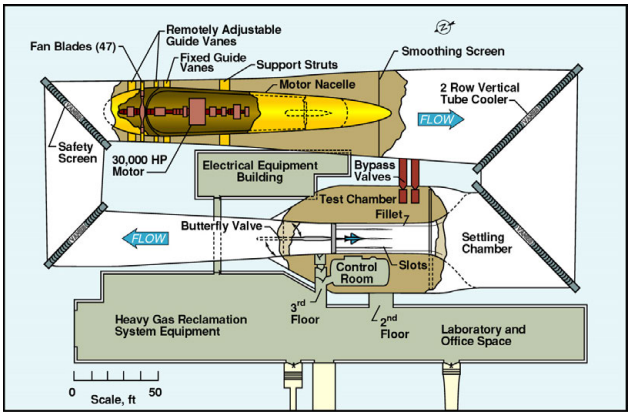

Fig. 14 Overview of the TDT [Source: NASA].

B. Test Envelope Constraints

The WT test envelope is restricted by several test article and system constraints. Boeing, NASA, and NextGen Aeronautics conducted extensive analysis of the WT test article and determined the maximum allowable operating conditions for the various components. Figure 15 overlays these constraints on top of the TDT test envelope. The following sections will elaborate on the constraints pictured in the figure.

1. Test article structural limits

The main driving constraints on the wind tunnel envelope are the structual limits of the wing spar, ribs, fuselage, nacelle, and mounting box assembly. Although the original objective was for all these components to be cleared to operate up to $M_\infty = 0.94$ and $q_\infty = 300$ psf, material limitations, design tradeoffs, and fabrication requirements resulted in the components having different restrictions. The mounting box assembly, nacelle, and fuselage were all cleared to operate up to $M_\infty = 0.94$ and $q_\infty = 300$ psf, which is represented by the orange dashed line in Fig. 15. The limiting test article components are the forward and aft ribs along the outboard part of the wing, which can only operate up to $M_\infty = 0.85$ and $q_\infty = 230$ psf with sufficient safety margins. These boundaries are shown by the red solid line in Fig. 15. As a result, due to structural limits the WT test article is restricted to test conditions at or below $M_\infty = 0.85$ and $q_\infty = 230$ psf.

2. Test article balance limits

In the shims-off configuration, the balance structural loads are an additional constraint to the test envelope. During testing in this configuration, loads will be continuously monitored to ensure load limits are not exceeded. These limits are summarized in Table 3.

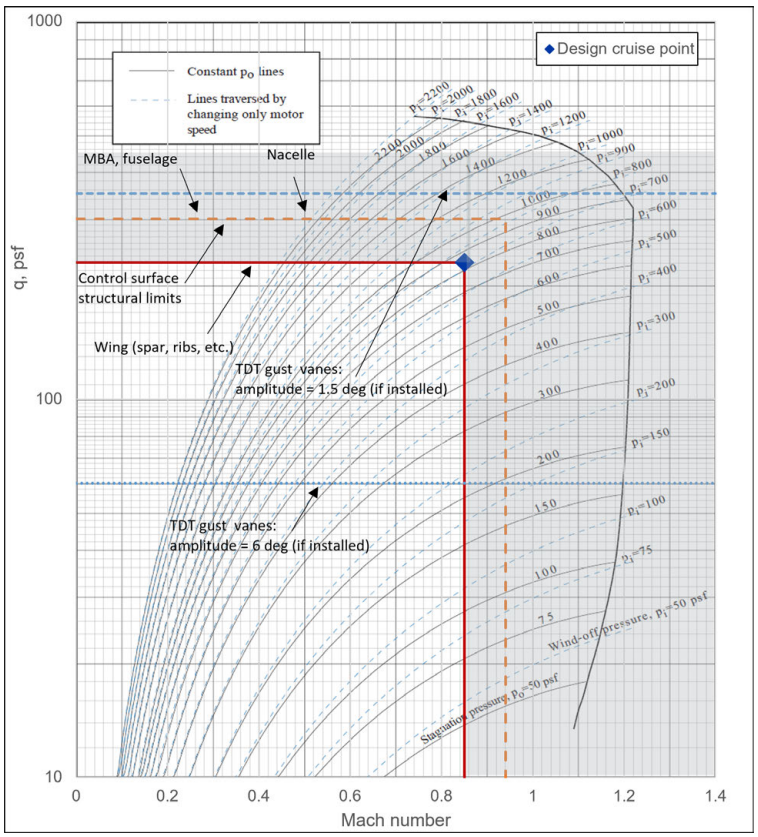

Fig. 15 WT test article constraints overlaid on the TDT test envelope.

Table 3 NASA balance 1637S load limits.

Component	Load
Normal force	5,700 lbs
Axial force	500 lbs
Pitching moment	15,000 in-lbs
Rolling moment	215,000 in-lbs
Yawing moment	15,000 in-lbs

3. Test article control surface limits

Another restriction on the test boundary is the safe operating limits of the control surfaces. As control surface deflections increase in magnitude, the load on the structural assembly will increase. The original intent was for all the control surfaces to be cleared to safely operate up to $M_\infty = 0.94$ and $q_\infty = 300$ psf with ±20 degrees of deflection. Since the size, location, and linkage kinematics of the control surfaces vary, the loads on the assemblies differ and the goal flight condition and deflection limits are not within the required structural safety limits for all surfaces. Ultimately, for the full desired deflection range, all the control surfaces could not be cleared to operate at dynamic pressures past 200 psf.

Instead, Boeing and NextGen Aeronautics analyzed the control surfaces at lower deflection angles of ±10 and ±15 degrees. These analyses determined that all the control surfaces are able to operate up to $M_\infty = 0.94$ and $q_\infty = 300$ psf within the allowable margins if the control surface deflections are restricted to ±10 degrees. This was not considered to be an issue for any of the planned open- or closed-loop testing. Therefore, the dashed yellow line in Fig. 15, corresponding to the goal envelope, is within the control surface structural limits when deflections are restricted to ±10 degrees.

Alongside the structural limits of the control surfaces, the control surface actuators also restrict the feasible test envelope. The hydraulic actuators, used to actuate the three ailerons, have sufficient capability such that they are not a limiting factor; the electric servos, however, are significantly easier to overload. Since part of the planned testing (aerodynamic characterization and drag optimization, for example) may require sustained, continuous movements of the control surfaces, Boeing and NASA decided to treat the continuous (rather than the peak) load limit as the operating limit for the electric servos. Enforcing this restriction will help prevent servo burnout and provide ample safety margins on the servo instantaneous load limits. The resulting deflection limits on the control surfaces are shown in Table 4, corresponding to the control surface naming convention shown in Fig. 5. For operation in the $M_\infty = 0.85$ and $q_\infty = 230$ psf envelope, the control surfaces are cleared to operate within the listed deflection ranges. The hydraulic actuators have significantly more capability and the limiting factors were simply the ±10 degree structural limits. The limits shown in Table 4 will be incorporated into the Boeing closed-loop controller as the saturation limits on the control surface commands.

Table 4 Maximum deflection range for the control surfaces at $M_\infty = 0.85$ and $q_\infty = 230$ psf.

	MPF1.1	MPF1.2	MPF1.3	A1	MPF2	MPF3	MPF4	MPF5	A2	A3
Minimum (deg)	-6	-5	-4	-10	-6	-6	-8	-10	-10	-10
Maximum (deg)	4	4	2	10	3	4	5	8	10	10

4. TDT limits

The TDT gust vanes provide an operational constraint upon the IAWTM test envelope. When they are installed during the GLA portion of testing, the dynamic pressure limit varies with gust vanes amplitude as shown in Fig. 15. If a larger 6 degrees amplitude is desired, the gust vanes are restricted to dynamic pressures at or below 60 psf. The max allowable dynamic pressure increases to 350 psf if the amplitude is restricted to 1.5 degrees.

C. Open-loop

Phase 1 of wind-on testing during the IAWTM experiment will focus on open-loop aerodynamic and aeroelastic characterization. Figures 16 provides a graphical representation of the two series that are planned for this portion of testing. Each series corresponds to a different initial wind-off pressure (p_i) line, which will be traversed from the lower left of the plot to the upper right by increasing the motor speed. At each of the dotted points along each curve, static schedules and dynamic sweeps of the control surfaces will be conducted to collect data that will be used for aerodynamic model verification and updating. In addition, these control surface tests will be conducted at several test article angles of attack.

Figure 16 also presents the primary, secondary, and tertiary test points at which the drag optimization, MLA, and GLA experiments will be run. While these points are all in the higher M_∞ and q_∞ quadrant of the test matrix, the lower subsonic and transonic test points are critical for anchoring the aerodynamic models and understanding when and how transonic aerodynamics may lead to modeling discrepancies.

The curves for test series 1 and 2 are represented again in Fig. 17 with the flutter boundaries for the shims-off (solid blue line) and shims-on (dashed blue line) configurations based on ZAERO flutter analyses shown in the upper right quadrant of the figure. For both of these configurations, the flutter mechanism is a hump mode with approximately 2–3 percent damping. Since several desired test points lie near or within the predicted flutter boundary for these test article configurations, and the as-built model structural damping is quite low, the real-time subcritical assessment of modal damping and predicted flutter dynamic pressure will be essential during this phase of testing. For reference, the flutter boundary for the flutter ballast configuration is shown in red.

1. Aerodynamic Characterization Testing

The first test sequences will be with the model in the shims-off configuration (balance on the load path) and follow test series 1 and 2 to collect experimental aerodynamic data. Each surface will be swept through their corresponding deflection ranges in discrete increments while angle of attack (AOA) is held constant. Interaction testing between neighboring surfaces will also be conducted if time allows. The same control surface sweeps will be repeated at multiple AOAs to produce an aerodynamic model of the control surfaces at each test condition.

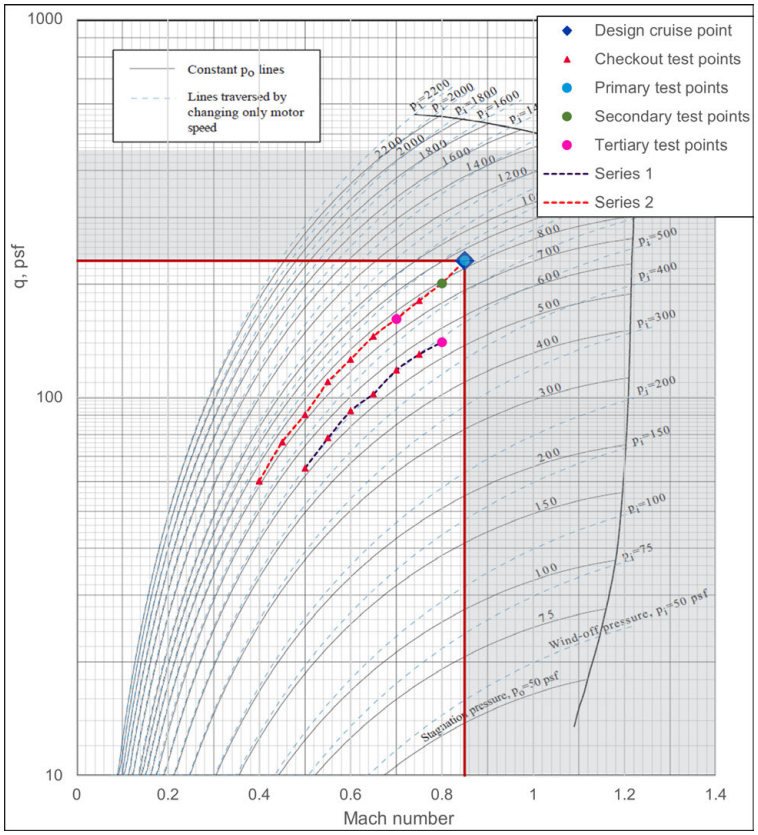

Fig. 16 Planned WT test points during phase 1.

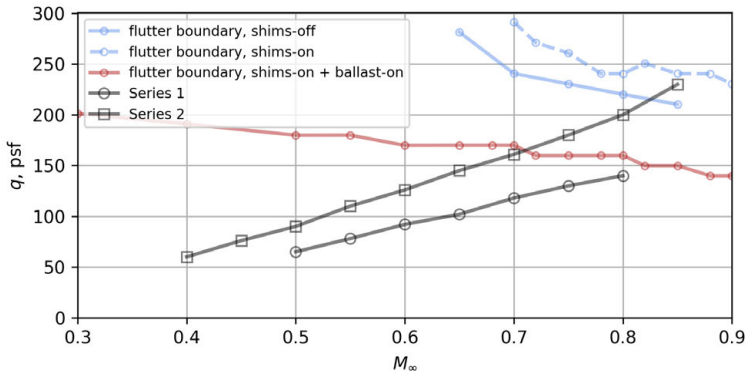

Fig. 17 Planned WT test series and ZAERO-predicted flutter boundaries.

The resulting experimental datasets will be compared against the extensive numerical simulations NASA has run using the test article OML. Fabrication tradeoffs in the as-built test article, such as control surface gaps and through-holes for servo pushrods, are difficult to model with CFD, and thus it is expected that the experimental values will differ from the numerical predictions. These tests will help to quantify the magnitude of the differences. In addition, the tests will produce an experimentally-derived aerodynamic model that will be incorporated into the simulation model and closed-loop drag optimization analysis.

2. Aeroelastic Characterization Testing

Following the aerodynamic characterization runs with the shims-off configuration, the model will be changed to the shims-on configuration, which removes the balance from the load path while leaving the OML unchanged. The same test series 1 and 2 will be run for this configuration and target aeroelastic characterization. NASA and Boeing have multiple tests planned for the aeroelastic characterization effort. Sine sweep chirps of each control surface will be performed at each of the primary, secondary, and tertiary test points. In order to capture any AOA dependencies, these tests will be repeated at multiple AOAs at the same test condition. Similar to the aerodynamic testing, a limited number of tests will be conducted with simultaneous chirps of neighboring surfaces to quantify interaction effects. NASA has also planned a sequence of control surfaces excitation tests using multisine inputs at the same test points as the chirp tests. In this method, described in Ref. [14] for a system identification study using CFD simulations of the IAWTM test article, testing efficiency may be improved since multiple surfaces are actuated simultaneously, thus reducing the number of total test points required. These tests will be compared against the more traditional chirp signals to compare results for data acquired in both methods.

Lastly, after the aeroelastic characterization testing with the shims-on configuration, a third set of open-loop tests will examine the shims-on, ballast-on configuration. These tests will be a truncated sequence of test series 2 since the intent during this phase is to avoid the flutter boundary. Limited aeroelastic characterization testing will be repeated with this configuration to quantify ASE response changes due to the installation of the flutter ballast.

D. Closed-loop

The primary focus of the first phase of testing is on open-loop characterization in order to validate and improve aerodynamic and aeroelastic models. These validated models will be critical to improve the developed WT control laws prior to the second phase of testing. This second phase will focus on closed-loop testing with the WT control system in the loop. Different controllers have been developed for each of the various test objectives by Boeing and NASA teams using both full- and WT-scale simulation models (for related work, see for example Refs. [10, 15–17]). Representative results for Boeing controllers developed in preparation for the WT experiment are discussed in this section, but test article limits discussed above are not reflected in all simulated results.

1. Drag Optimization

The first of the closed-loop test objectives is drag optimization. Boeing has developed a fuel-burn minimization controller for the nominal full-scale aircraft to operate alongside the baseline longitudinal, lateral-direction, and throttle controllers. The fuel-burn optimization controller commands the aircraft control surfaces to reduce fuel burn, while the baseline control laws maintain level flight. Figure 18 depicts the C_L, C_D, AOA, and fuel-flow during a simulation of the nominal full-scale aircraft at the design cruise condition with the fuel-burn optimization control active. Although the full-scale vehicle design has additional control surfaces, they have been grouped together here to match those in the WT test article as depicted in Fig. 5. The control surface deflections in Fig. 19 are optimized in real-time to produce a lower fuel-flow measurement, and simultaneously the baseline longitudinal control law deflects the elevator to change AOA to compensate for the change in C_L. Eventually, the aircraft settles into a new set of trim control surface deflections at a slightly higher AOA. Note that the net C_L is still the same, but the fuel-flow measurement and C_D have decreased slightly.

Fuel-flow measurements are not available in a WT test, so the same controller cannot be directly copied for subscale WT testing. As seen in Fig. 18 above, drag is lower when the fuel-flow is minimized, so the WT controller objective is changed to drag minimization. Additionally, since the test article is not free-flying and there is no horizontal stabilizer, the baseline longitudinal and lateral-directional control laws no longer apply. The challenge with the absence of baseline longitudinal control laws is that they indirectly control AOA via the elevator to maintain a constant C_L to keep the aircraft trimmed for 1-g flight.

In the TDT, the test article pitch angle is manually controlled by the tunnel operator. For these drag optimization tests, a second control law is added to the controller to return AOA commands at a very low rate. This second control law attempts to maintain constant C_L by changing AOA, simulating the baseline longitudinal control law in the nominal full-scale aircraft. Since the test article pitch angle is manually controlled, these AOA commands are sent to the tunnel operators, who will then command the model to the desired angle. Due to system and operator rate limits, the AOA commands are sent in discrete increments at a low rate.

Figures 20 and 21 depict the drag optimization controller during a simulation of the WT test article at $M_\infty = 0.85$ and $q_\infty = 230$ psf. To fully close the loop, the human-in-the-loop control of model pitch angle is approximated with

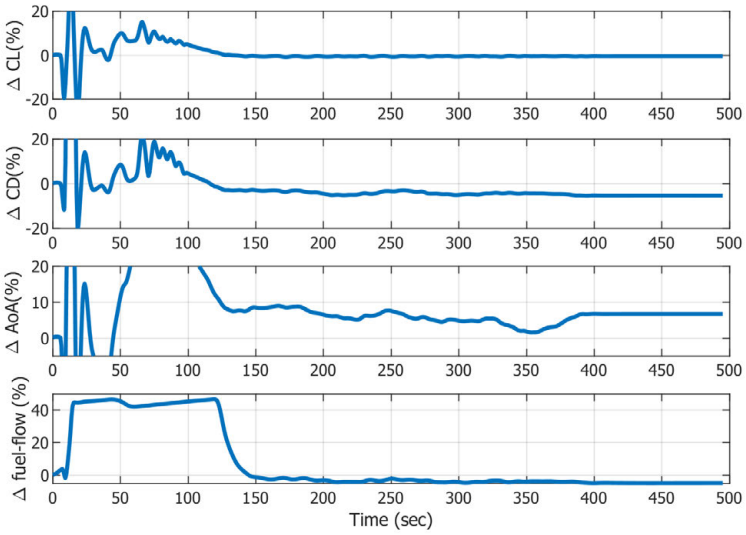

Fig. 18 Percent change in C_L, C_D, AOA, and fuel-flow during a simulation of the fuel-burn optimization control law at $M_\infty = 0.85$, $q_\infty = 230$ psf with the nominal full-scale aircraft.

a discrete-time filter and heavily-damped second-order response. The plots show the control surfaces moving as the controller attempts to minimize C_D while maintaining constant C_L. By the end of the simulation, the controller has converged to a lower C_D with a higher AOA. Note that the aerodynamic model in the simulation contained minimum drag at ±5 degree deflection breakpoints, so the controller has successfully converged towards the minimum drag point with the current aerodynamic model. The outboard-most ailerons are not used for drag optimization, so they remain fixed at zero and are not plotted.

2. Maneuver Load Alleviation

A second test objective is the demonstration of active MLA. In a nominal full-scale aircraft, the MLA control law is based upon load factor. As the aircraft pitches up or down, the control surfaces deflect to minimize the bending moments experienced at critical points on the aircraft, such as the wing root. For the test article, the general architecture is the same, but the variables are different to reflect the available measurements. For example, the goal of the WT controller is to minimize strain gauge measurements, particularly at the inboard-most strain gauge location (SG01). Likewise, there is not a direct load factor measurement available to trigger the MLA controller. Instead, the full-scale aircraft trim C_L values are used as the basis for 1-g loads. In order to simulate a pushover or pull-up maneuver, the TDT operator will use the model pitch angle to change C_L.

Figures 22 and 23 depict the MLA controller during a simulation of the test article at $M_\infty = 0.80$ and $q_\infty = 140$ psf. The simulation initializes with the test article at trim before the model pitch angle is increased to double the lift coefficient, simulating a 2-g pull-up maneuver. For this simulation, the control surfaces are grouped into two sets: one group of inboard surfaces (MPFs 1.1, 1.2, and 1.3 and A1) and a second group of outboard surfaces (MPFs 2, 3, 4, and 5 and A2). The outboard-most A3 is not used for MLA. As can be seen in the bottom plot of Fig. 23, the control surfaces move to shift the load inboard, which decreases the net bending moment experienced near the wing root as shown by the root strain gauge, SG01, shown in the top plot of Fig. 23.

3. Gust Load Alleviation

The third test objective is GLA. Current research work has explored the use of forward-looking light detection and ranging (LIDAR) installed on the aircraft to measure wind velocity a set distance in front of the aircraft. These LIDARs can measure the wind and detect gusts immediately before the aircraft encounters them. The control surfaces can then be employed to preemptively counteract the gusts to reduce the resulting loads and improve ride quality.

For the WT experiment, wind gusts will be generated by the two pairs of gust vanes that sit upstream of the WT test

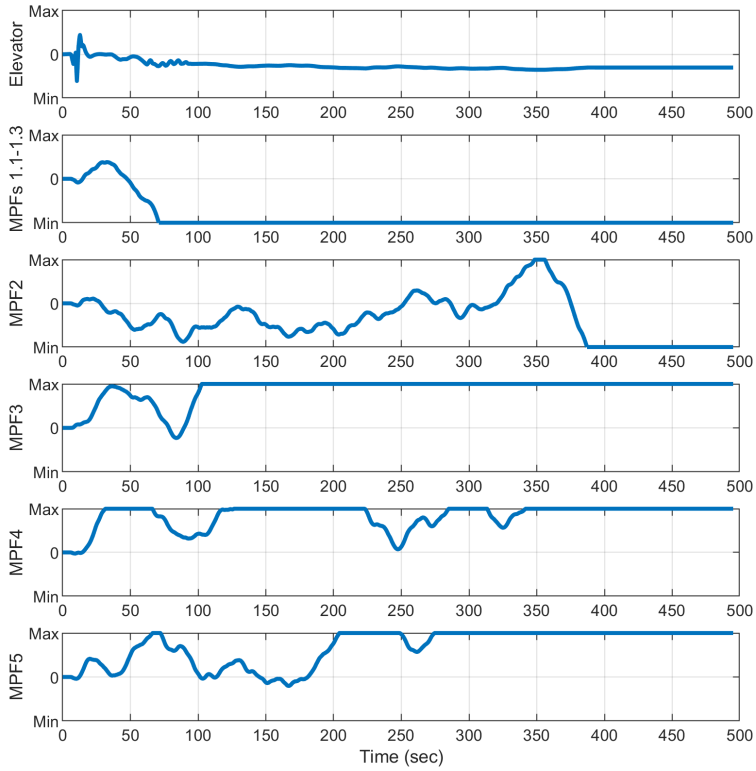

Fig. 19 Control surface positions during a simulation of the fuel-burn optimization control law at $M_\infty = 0.85$, $q_\infty = 230$ psf with the nominal full-scale aircraft. Note that the MPF surfaces are symmetric for both wings and are restricted to move only a quarter of their full deflection range during fuel-burn optimization.

article, as shown in Figure 24. While a forward-looking LIDAR will not be used during this experiment, an upstream vane sensor will be installed ahead of the test section to measure the gust immediately upstream of the model and serve as a surrogate for the forward-looking LIDAR sensor. Figures 25 and 26 depict the response of the test article with and without GLA active during a simulation at $M_\infty = 0.70$ and $q_\infty = 190$ psf with the upstream gust vanes oscillating at a fixed frequency and amplitude. As seen in Fig. 25, the peak strain at the root full-bridge strain gauge (SG01) is roughly 4-percent lower while GLA is active versus when it is not.

4. Active Flutter Suppression

Lastly, the fourth test objective is to demonstrate AFS. These tests will be done with the flutter ballast installed to lower the dynamic pressure at which the hard flutter mechanism is predicted to occur. Due to the need to change the model configuration and the overall risk of flutter testing, this will be the last set of tests in Phase 2.

The flutter controller is designed to suppress the unstable aeroelastic modes. As such, the open-loop characterization done in Phase 1 will be critical to producing accurate state-space models of the test article at the test conditions leading up to the flutter boundary. The Phase 2 closed-loop test sequence will approach this flutter boundary and demonstrate the suppression of aeroelastic instabilities.

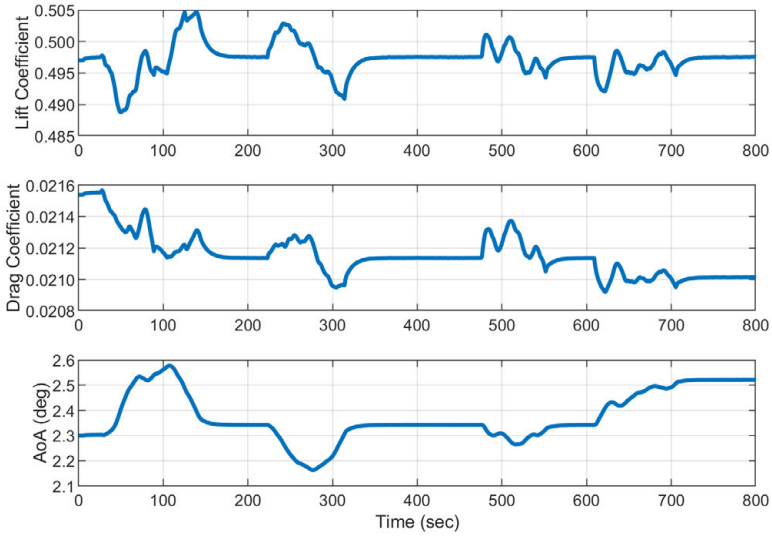

Fig. 20 C_L, C_D, **and AOA during a simulation of the drag optimization control law at** $M_\infty = 0.85$, $q_\infty = 230$ **psf for the shims-off configuration.**

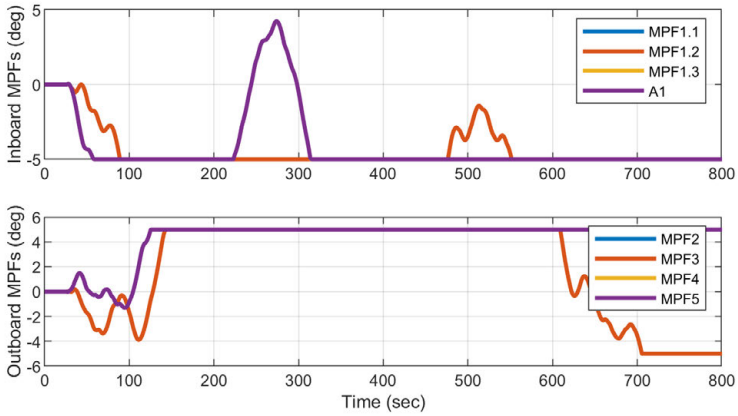

Fig. 21 Inboard and outboard control surface positions during a simulation of the drag optimization control law at $M_\infty = 0.85$, $q_\infty = 230$ **psf for the shims-off configuration.**

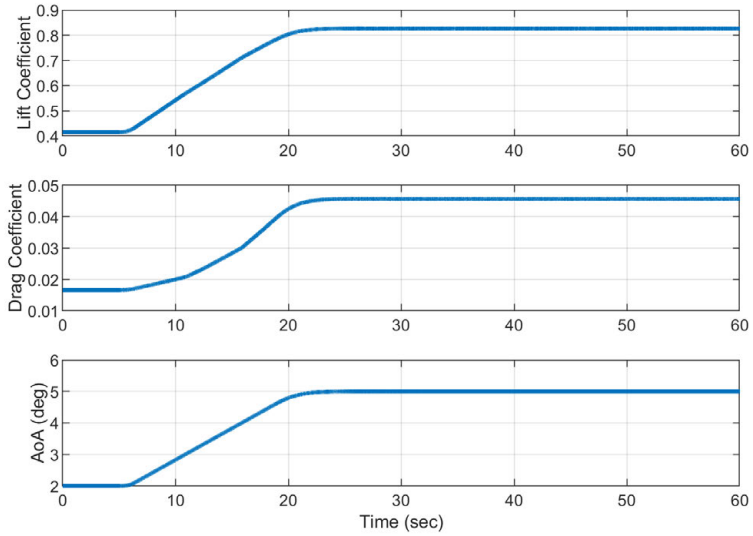

Fig. 22 C_L, C_D, **and AOA during a simulation of the MLA control law at** $M_\infty = 0.80$, $q_\infty = 140$ **psf for the shims-on configuration.**

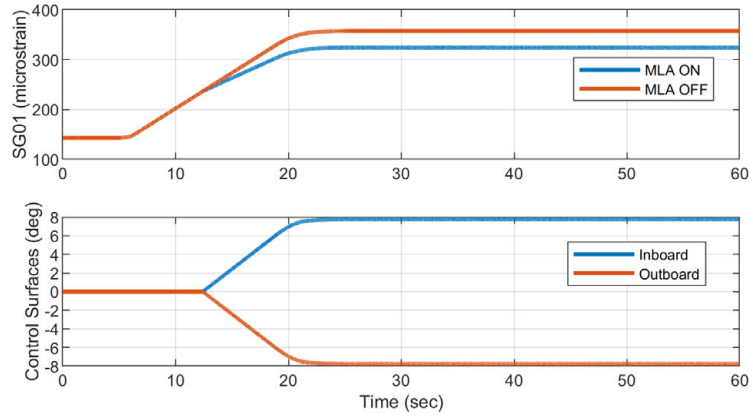

Fig. 23 Strain gauge SG01 measurements and control surface positions during a simulation of the MLA control law at $M_\infty = 0.80$, $q_\infty = 140$ **psf for the shims-on configuration.**

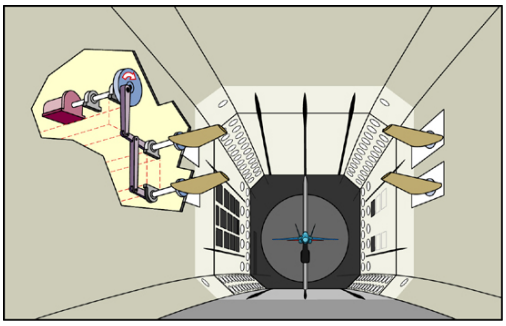

Fig. 24 Overview of AOS gust vane locations relative to the WT test section [Source: NASA].

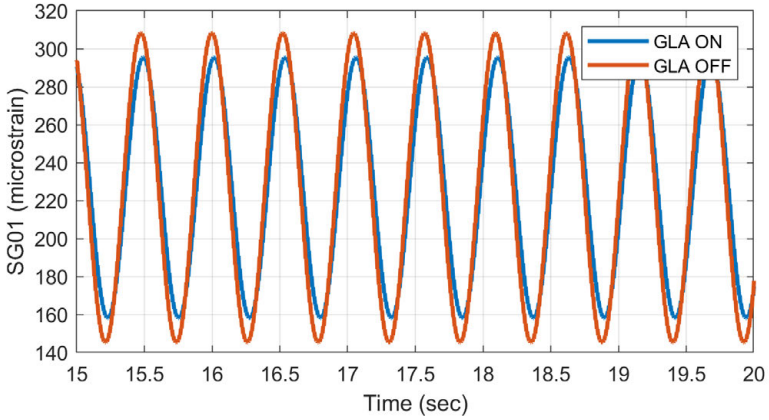

Fig. 25 Strain gauge SG01 measurements with and without GLA active during a simulation at $M_\infty = 0.70$, $q_\infty = 190$ psf for the shims-on configuration.

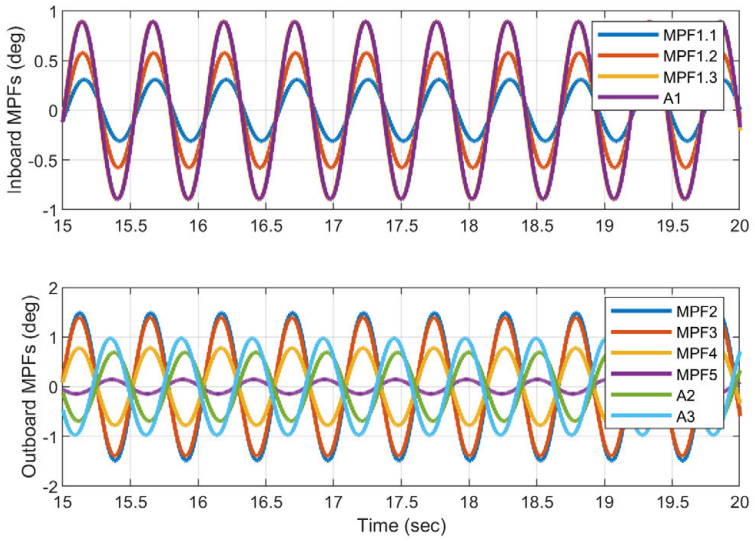

Fig. 26 Control surface positions while GLA is active during a simulation at $M_\infty = 0.70$, $q_\infty = 190$ psf for the shims-on configuration.

V. Conclusion

In this paper, an overview of the Integrated Adaptive Wing Technology Maturation (IAWTM) wind-tunnel test article is provided, to include discussion related to model scaling, structural design, instrumentation, and control systems. Completed and planned characterization activities are described, as well as Phase 1 test plans, during which the open-loop characterization tests will be conducted. Details related to test article and facility test envelope constraints are also discussed. Representative results for several closed-loop simulations targeting the primary control objectives, which will be tested during Phase 2 of the experiment, are also presented and discussed. Lessons learned and data acquired during the preparation and conduct of the IAWTM WT experiment will be directly applicable to improvements in aeroelastic modeling and testing of high aspect ratio, highly flexible wings.

Acknowledgments

This work is supported by the NASA Advanced Air Transport Technology (AATT) Project. The authors would like to acknowledge significant contributions over many years to this project and the work presented in this paper by team members from Boeing, NextGen Aeronautics, and NASA.

References

[1] Brooks, T. R., Kenway, G. K., and Martins, J. R., "Benchmark Aerostructural Models for the Study of Transonic Aircraft Wings," *AIAA Journal*, Vol. 56, No. 7, 2018, pp. 2840–2855. https://doi.org/10.2514/1.J056603.

[2] Vassberg, J. C., Dehaan, M. A., Rivers, M., and Wahls, R. A., "Development of a Common Research Model for Applied CFD Validation Studies," *26th AIAA Applied Aerodynamics Conference*, 2012. https://doi.org/10.2514/6.2008-6919.

[3] Heaney, P. S., Ivanco, T. G., and Bilgen, O., "Distributed Sensing of a Cantilever Beam and Plate using a Fiber Optic Sensing System," *AIAA Aviation 2018*, Atlanta, GA, 2018. https://doi.org/10.2514/6.2018-3482.

[4] Anderson, W. K., Biedron, R. T., Carlson, J.-R., Derlaga, J. M., Diskin, B., Druyor Jr., C. T., Gnoffo, P. A., Hammond, D. P., Jacobson, K. E., Jones, W. T., Kleb, B., Lee-Rausch, E. M., Liu, Y., Nastac, G. C., Nielsen, E. J., Padway, E. M., Park, M. A., Rumsey, C. L., Thomas, J. L., Thompson, K. B., Walden, A. C., Wang, L., Wood, S. L., Wood, W. A., and Zhang, X., "FUN3D Manual: 14.0.2," NASA TM-20230004211, 2023.

[5] Waite, J., Bartels, R. E., and Stanford, B., "Aeroelastic Model Development for the Integrated Adaptive Wing Technology Maturation Project Wind-Tunnel Test," *AIAA Aviation 2020*, 2020, p. 2717. https://doi.org/10.2514/6.2020-2717.

[6] Bartels, R. E., and Chwalowski, P., "Computational Fluid Dynamics Simulations of the Transonic Dynamics Tunnel Airstream Oscillators," *AIAA SciTech 2021*, 2021. https://doi.org/10.2514/6.2021-0835.

[7] Bartels, R. E., "High Fidelity Adaptively Refined CFD and Reduced Order Models of the Integrated Adaptive High Aspect Ratio Wing Wind Tunnel Model," *AIAA Aviation 2023*, 2023, p. 3240. https://doi.org/10.2514/6.2023-3240.

[8] McDonald, R. A., and Gloudemans, J. R., "Open Vehicle Sketch Pad: An Open Source Parametric Geometry and Analysis Tool for Conceptual Aircraft Design," *AIAA SciTech 2022*, San Diego, CA, 2022. https://doi.org/10.2514/6.2022-0004.

[9] Xiong, J., Nguyen, N. T., Stanford, B., and Bartels, R. E., "Aeroelastic Modeling and CFD Simulation of Wind-Tunnel Scale Aspect Ratio 13.5 Common Research Model," *AIAA Aviation 2021*, 2021, p. 2527. https://doi.org/10.2514/6.2021-2527.

[10] Waite, J., Grauer, J. A., Bartels, R. E., and Stanford, B., "Aeroservoelastic Control Law Development for the Integrated Adaptive Wing Technology Maturation Wind-Tunnel Test," *AIAA SciTech 2021*, 2021. https://doi.org/10.2514/6.2021-0609.

[11] Grauer, J. A., "Method for Real-Time State Estimation of Structural Modes for an Aeroelastic Wind Tunnel Model," *AIAA SciTech 2021*, 2021. https://doi.org/10.2514/6.2021-1643.

[12] MSC Software Corporation, *MSC Nastran Aeroelastic Analysis User's Guide*, 2021.

[13] ZONA Technology, Inc., *ZAERO v. 9.3 User's Manual*, 2019.

[14] Grauer, J. A., Waite, J., and Stanford, B., "Reduced-Order Aerodynamic Modeling Based on CFD Frequency Responses from Multisine Inputs," *AIAA SciTech 2021*, 2021, p. 1423. https://doi.org/10.2514/6.2021-1423.

[15] Hartwell, B., and Nguyen, N. T., "Nonlinear 6-DoF Simulations of a Multi-Objective Optimal Flight Control System for Flexible Wing Aircraft," *AIAA SciTech 2021*, 2021, p. 1117. https://doi.org/10.2514/6.2021-1117.

[16] Nguyen, N. T., and Xiong, J., "Real-time Drag Optimization of Aspect Ratio 13.5 Common Research Model with Distributed Flap System," *AIAA SciTech 2021*, 2021, p. 0069. https://doi.org/10.2514/6.2021-0069.

[17] Forte, C., Nguyen, N. T., Xiong, J., and Sager, J., "Real-Time Drag Optimization and Maneuver Load Alleviation Control for a High Aspect Ratio Wing Wind Tunnel Model," *AIAA SciTech 2022*, 2022, p. 0715. https://doi.org/10.2514/6.2022-0715.